β-delayed charged-particle decay of ^{22,23}Si

A. A. Ciemny,[1,*] C. Mazzocchi,[1,†] W. Dominik,[1] A. Fijałkowska,[2,1] J. Hooker,[3,4] C. Hunt,[3,4] H. Jayatissa,[3,4] Ł. Janiak,[5,1] G. Kamiński,[6] E. Koshchiy,[3] M. Pfützner,[1] M. Pomorski,[1] B. Roeder,[3] G. V. Rogachev,[3,4] A. Saastamoinen,[3] S. Sharma,[1] N. Sokołowska,[1] W. Satuła,[1] and Jagjit Singh[1]

[1]*Faculty of Physics, University of Warsaw, 02-093 Warsaw, Poland*
[2]*Department of Physics and Astronomy, Rutgers University, New Brunswick, New Jersey 08903, USA*
[3]*Cyclotron Institute, Texas A&M University, College Station, Texas 77843, USA*
[4]*Department of Physics and Astronomy, Texas A&M University, College Station, Texas 77843, USA*
[5]*National Centre for Nuclear Research, 05-400 Otwock, Świerk, Poland*
[6]*Heavy Ion Laboratory, University of Warsaw, 02-093 Warsaw, Poland*

(Received 20 June 2021; revised 24 May 2022; accepted 13 July 2022; published 28 July 2022)

The β decay of ^{22,23}Si by emission of delayed charged particles was investigated in an experiment at the Cyclotron Institute of Texas A&M University by means of an optical-readout time-projection chamber. The previously-known decay of the two isotopes by β-delayed one- and two-proton emission was confirmed. For the first time, a new, rare, decay mode for ^{23}Si, β-delayed three-proton emission, was observed and β-delayed proton-α emission tentatively identified. Moreover, the β-decay pattern for the ground state of ^{23}Si was studied by means of multireference density-functional-rooted calculations.

DOI: 10.1103/PhysRevC.106.014317

I. INTRODUCTION

Neutron-deficient nuclei located at the edges of stability, close to the proton drip-line are characterized by large Q-value windows and their respective daughters by low separation energy for charged-particle(s) (one, two, and three protons, α and proton-α) emission. Moreover, the isobaric analogue state (IAS) in the daughter nucleus is often unbound with respect to such (multi)particle emission. β decay of these very exotic nuclei is likely to populate excited states often well above the particle-separation energy in the daughter nucleus. Consequently, charged particles can be emitted promptly after the β particle. This combination of properties results in large probabilities for emission of one, two, three protons, αs and proton-α promptly after β decay (βp, $\beta 2p$, $\beta 3p$, $\beta\alpha$, and $\beta p\alpha/\beta\alpha p$, respectively) [1,2]. In the case of population of levels close to the proton-separation energy, γ de-excitation will compete with (delayed) proton emission.

The study of delayed charged-particle(s) emission provides a unique window into the structure of highly unbound states in these exotic nuclei. The spin selectivity of the β decay can in fact provide a different and complementary point of view to the one offered by nuclear reaction investigations.

A fertile ground for these studies is the region of $Z > N$ nuclei with $A = 20$–30, where several very rare decay modes are energetically possible. A sizable amount of the decay strength of such nuclei will proceed through the IAS in the daughter nucleus, which is in most cases located well above the particle-separation energies. As a consequence, a large portion of the delayed particle(s) emission will proceed from the IAS. Nevertheless, the study of decays by delayed particles can allow also to shed light into excited states in the daughter nucleus both above and below the IAS, states that are fed by Gamow-Teller transitions. It has been demonstrated, e.g., that β-delayed multiproton emission of very exotic nuclei can be used to probe the β-decay strength in the high-energy end of the Q-value window, where excited states are particle unbound [3,4]. Moreover, it can happen that the very existence of these rare decay modes, like $\beta 3p$ or $\beta p\alpha/\beta\alpha p$, can shed light into local structure effects. In a recent publication, Lund *et al.* [5] have investigated the systematic behavior of β-delayed charged particle emission in ^{21}Mg and neighboring nuclei along the $T_Z = -1$ and $T_Z = -3/2$ lines. In their work, the authors interpret the systematic trends in β-delayed charged particle decay as due to odd-even effects in the decay energies rather than nuclear structure ones, like clustering. A test of such conclusion can be obtained by looking for these exotic decay modes in heavier and more exotic $T_Z = -5/2$ isotopes, like ^{23}Si and ^{27}S.

In this context, a new study of β-delayed charged particle decay of ^{22,23}Si was conducted and is reported here. ^{23}Si is the lightest $T_Z = -5/2$ isotope known to date. It was first observed in the fragmentation of a ^{40}Ca beam at GANIL [6]. The first decay data were obtained about 10 years later, when its βp and $\beta 2p$ decay was studied [7]. The decay of ^{23}Si is dominated by transitions to the IAS, with part of the strength feeding lower-lying states in Gamow-Teller (GT) decay. Emission of delayed protons from the IAS and from lower states populated in GT transitions was observed and 16 transitions identified. Moreover, the half-life was determined

*aleksandra.ciemny@fuw.edu.pl
†chiara.mazzocchi@fuw.edu.pl

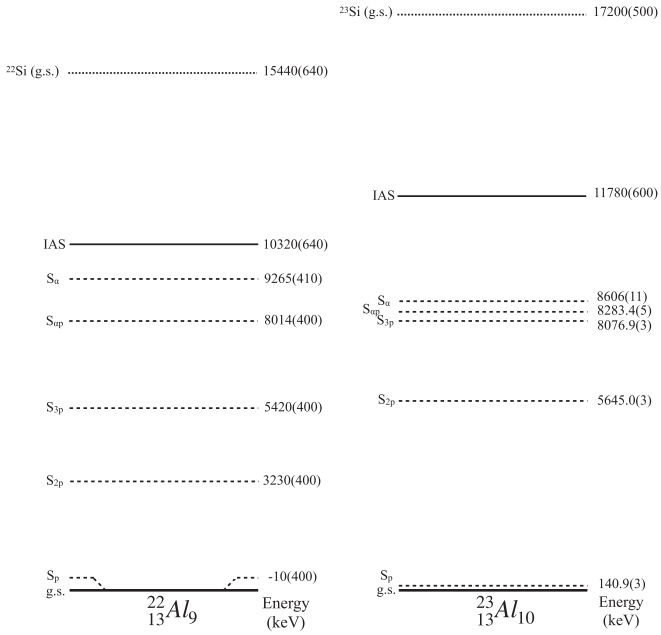

FIG. 1. Ground-state (g.s.) energies for the $A = 22,23$ silicon precursors (dotted lines) [16], particle-separation (dashed lines) [16], and IAS (solid lines) [7,17] energies for the respective aluminium daughter nuclei ($A = 22,23$).

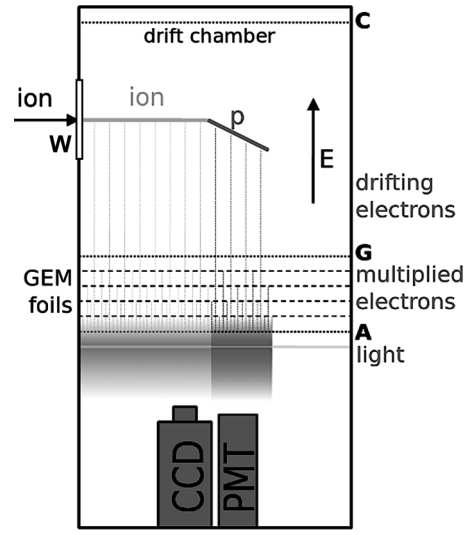

FIG. 2. Schematic representation of the OTPC detector and its working principle. The beam-entrance window is highlighted on the side of the chamber (W) and the cathode (C), gating electrode (G) and anode (A) are shown as dotted lines. The GEM foils as dashed lines. The ion enters the chamber with a kinetic energy of about 10A MeV and is stopped in the active volume of the chamber. See text for details.

and the position of the IAS in the daughter ^{23}Al inferred. More recently, a new study detected both protons and γ rays following β decay, allowing for β-proton-γ coincidences to be established. One new transition was added and the previous observation of the β2p decay branch confirmed [8]. The low-energy structure of the daughter ^{23}Al has been studied also by means of nuclear reactions in several works [9–11]. None of the studies could identify more exotic decay paths for this nucleus, like $\beta 3p$ and $\beta p\alpha/\beta\alpha p$.

The $T_Z = -3$ isotope ^{22}Si was also discovered at GANIL as a product of ^{36}Ar fragmentation [12]. First insight into its decay properties was obtained a decade later, when its half-life was determined and its βp decay branch observed with five proton-transitions identified [13]. The β2p decay path could not be firmly established at that occasion. Emission of $\beta 2p$ from its IAS was recently discovered, together with a new βp transition [14]. ^{22}Si was also reported to show a large mirror asymmetry in its decay, although with very big uncertainties [15].

In Fig. 1 the energetic of the decay channels open for the two isotopes investigated in this work, ^{22,23}Si, is summarized.

II. EXPERIMENT

The measurement of the β-delayed charged-particle emission from ^{22,23}Si was conducted at the Cyclotron Institute of Texas A&M University, College Station (TX), USA. A ^{28}Si beam was accelerated to 45A MeV by the K500 superconducting cyclotron and impinged on a 150 μm-thick nickel target. The ^{22,23}Si ions so produced were separated from the rest of the reaction products by the momentum achromat recoil separator (MARS) [18]. Two ion-optics configurations of MARS were used during the course of the experiment, each optimised for transmission of ^{23}Si and ^{22}Si, respectively. Initially, during the beam tuning phase, a 300 μm-thick silicon detector, segmented along the vertical (y) direction, was inserted at the focal plane for diagnostics purposes. The ions reaching the focal plane of MARS were then identified on an event-by-event basis by plotting the energy-loss (ΔE) vs y-position matrix (MARS is dispersive in y) [19]. The cocktail beam obtained was mostly composed of the ion of interest, ^{23}Si or ^{22}Si, with some ^{20}Mg ($\sim$13%) and ^{23}Si ($\sim$40%), respectively. After the initial optimization of the spectrometer, the detector was removed to allow for the beam to reach the detection set up placed downstream.

The secondary beam entered then the detection set-up composed of the Warsaw optical time-projection chamber (OTPC) [20,21] through a 300 μm-thick silicon detector, which was placed just in front of it. The beam ions were then implanted in the OTPC, where they subsequently decayed. The OTPC is a gas-filled detector with an active volume 33 cm deep, 20 cm wide, and 21 cm high, which is immersed in an homogenous vertical electric field (143 V/cm). The separated and identified exotic ions enter the chamber horizontally, perpendicular to the field lines, though a window (see Fig. 2). The electrons generated in the ionization process by the interaction of the heavy ions and their charged-particle decay products (protons and α particles, while β electrons do not deposit enough energy to be detected) drift at a constant velocity in the electric field towards an amplification structure based on a set of four gas-electron multiplier (GEM) foils [22] and the anode. Light is generated in this process, which is recorded by a CCD camera (1024 pixels $\times$ 1024 pixels) and a photo-multiplier tube (PMT), see Fig. 2. By combining the

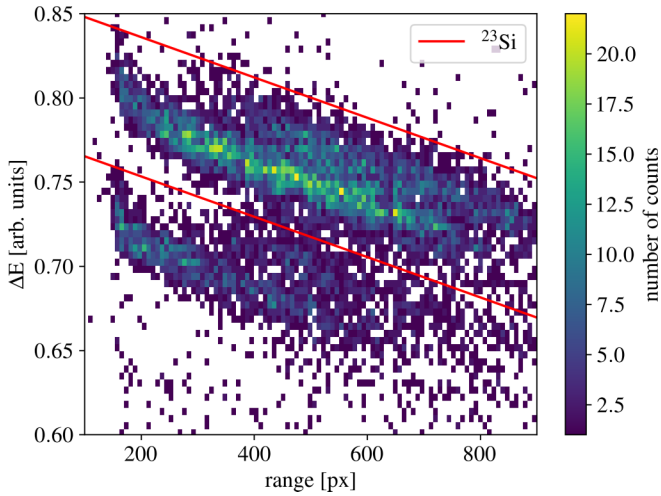

FIG. 3. Identification plot ΔE versus range for the ion-optics setting centered on ^{23}Si. Only events contained between the two red lines were considered in the analysis. See text for details.

information from the CCD image (projection of the particle trajectory on the horizontal plane) and the time-distribution of the light collected by the PMT tube (projection of the particle trajectory along the field direction), the trajectory of the particle can be reconstructed in three dimensions (3D). This is possible since the electron drift velocity and the stopping power for the particles in the gas are known. In this measurement a gas mixture consisting of He 69% + Ar 29% + CF_4 2% at atmospheric pressure was used, and the stopping power was calculated by using the SRIM suite [23]. The average electron drift velocity in the experiment conditions was measured to be $v_{\text{drift}} = 1.17(2)$ cm/μs. Temperature and pressure at the chamber were also monitored during the course of the experiment.

In order to reduce the amount of data collected, only the ions of interest and a small amount of other isotopes present in the cocktail beam were allowed to trigger the system and be recorded by the data acquisition system (so-called "good" ions). Such selection was achieved by setting a gate on the ΔE signal. The CCD camera ran continuously 65 ms frames (waiting time) while waiting for a good ion to trigger the system. Upon trigger, the beam was switched off while waiting for the decay to happen and the camera exposition time (T_{exp} or decay-time observation window) extended to 150 ms. The same T_{exp} value was used for both the ^{22}Si and ^{23}Si measurements. The beam was kept off for 1.5 s after the trigger to allow also for the data to be read out at the end of the T_{exp} window. Fast oscilloscopes recorded the PMT signal as well as signals necessary for ion identification (ΔE) and the camera control signals (start and stop of the camera exposition). The oscilloscopes were then read out together with the images after each triggering event, at the end of the T_{exp} window. At the end of readout, the beam was switched on again until the next trigger. In order to protect the detector from the charge deposited in the active volume by the heavy ions, a dual-sensitivity running-mode was employed. A gating electrode placed just above the amplification structure, at the anode-end of the drift volume and before the GEMs foils (see Fig. 2), is used for changing the detector sensitivity. The voltage on this electrode is set to a value that allows for observation of the heavy ions entering the chamber while avoiding

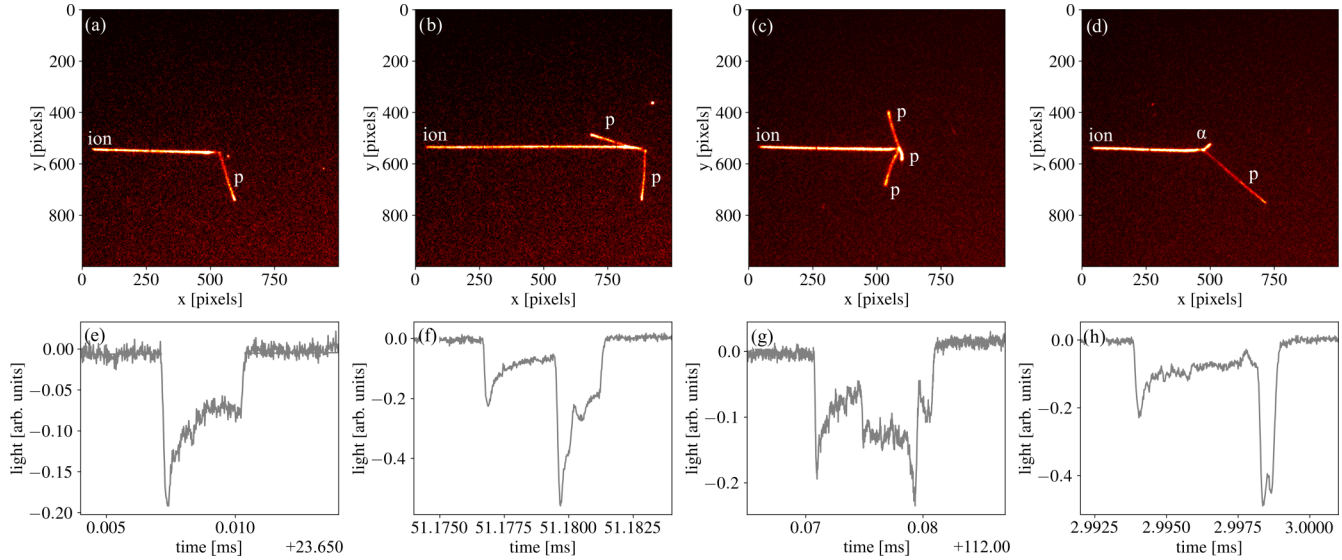

FIG. 4. Top panel: CCD images for example events of (a) βp, (b) $\beta 2p$, (c) $\beta 3p$, and (d) $\beta p\alpha$ decay of ^{23}Si. The horizontal track from left to right in each image corresponds to the ^{23}Si ion entering the chamber. The tracks emerging from the ion stopping point correspond to the emitted particles. Bottom panels: respective PMT signals for the (e) βp, (f) $\beta 2p$, (g) $\beta 3p$, and (h) $\beta p\alpha$ decay events. The signal generated by the ^{23}Si ion stopped in the chamber is not visible in the histograms displayed in the bottom panel. Only the portion of the PMT signal centered around the time at which the decay happened is shown. In the case of a single particle recorded in the decay, the PMT signal shows the corresponding Bragg peak. In the βp event in (a) and (e), the proton was emitted downwards, towards the anode. In the case of more particles emitted at the same time, as is for $\beta 2p$, $\beta 3p$, and $\beta p\alpha$, the PMT signal will be the convolution of the signals corresponding to each of the particles emitted.

TABLE I. The total branching ratios for the observed decay channels of ^{23}Si.

channel	Events	Branching
$\beta 1p$	5643	81.8(11)%
$\beta 2p$	533	7.73(35)%
$\beta 3p$	2	$2.9(^{+38}_{-19}) \times 10^{-2}$%
$\beta p\alpha$	1	$1.4(^{+33}_{-12}) \times 10^{-2}$%

overload of the amplification structure (so-called "low-sensitivity" mode). When a trigger is generated, the voltage applied to this electrode is changed within 20 μs so to be able to observe weaker-ionization particles, like low-energy protons or αs (so-called "high-sensitivity" mode). After the end of the $T_{\rm exp}$ window, the detector is returned to the low-sensitivity mode.

Ion-by-ion identification of the nuclear species triggering the detection set-up and entering the chamber was achieved by measuring ΔE in the silicon detector positioned just in front of the OTPC as a function of the range of the ions in the OTPC itself. In Fig. 3 the identification plot for the ions triggering the data acquisition for the spectrometer setting optimised for transmission of ^{23}Si is shown. In the figure, the events included between the two continuous red lines are identified as ^{23}Si ions, while those below the lower of the two lines are due to an about 50/50 mixture of ^{20}Mg and ^{23}Si activities. Each of the two main activity groups shows inside two subgroups of events with different ranges for the same isotopes. Such effect is due to the fact that the OTPC kapton beam-entrance window is covered by strips (7 mm-high, with 3 mm between adjacent strips, each consisting of 5 μm of Cu and 2 μm of Au) that form the electrodes of the drift cage and that the beam-spot was broader than one strip.

III. RESULTS AND DISCUSSION

A. ^{23}Si

1. Branching ratios and half-life

Events corresponding to ^{23}Si ions which triggered the data acquisition and stopped in the active volume of the detector were considered for further analysis. They correspond to the events contained between the two red lines in Fig. 3 and stopped between 10% and 90% of the range, i.e., between pixels 100 and 900. The latter condition was imposed to make sure that the decay of the ions by charged-particle emission would not be missed. A total of 7497 ^{23}Si ions met these requirements. The analysis of the images and of the respective PMT trace allowed to identify four decay branches for this isotope. Namely, decay with emission of one- and two- protons was confirmed, decay by emission of delayed three protons observed for the first time and by emission of a proton and an α particle tentatively established. In Fig. 4 example decay events with particle emission are shown, while in Table I the statistics gathered and the branching ratio for each decay mode are summarised. The branching ratios values reported take into account the finite-time observation window, which gives a 92.0(2)% probability to observe any ^{23}Si decay within

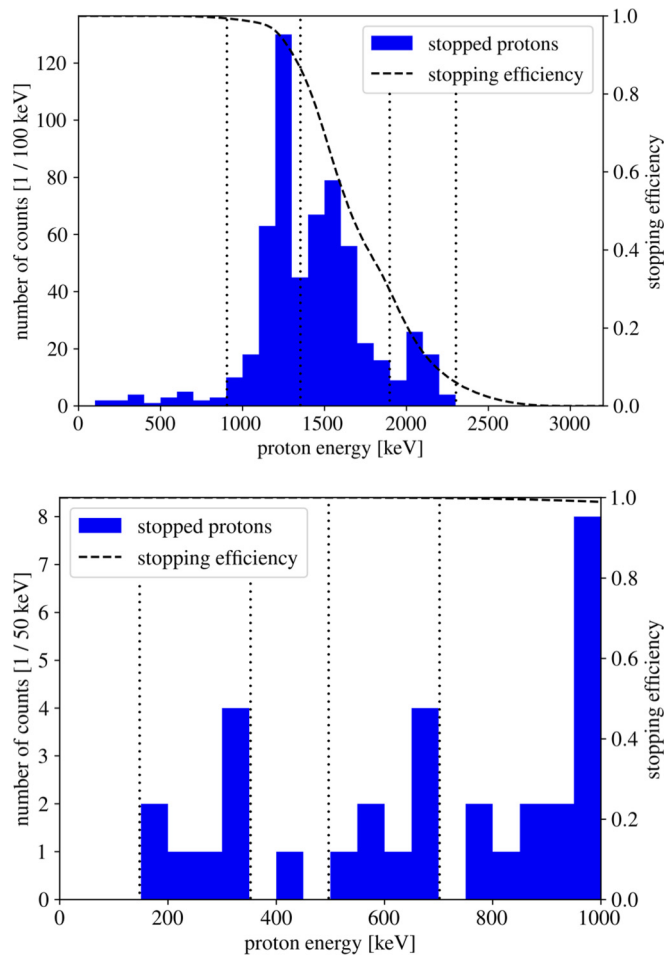

FIG. 5. Upper panel: Energy spectrum for protons following ^{23}Si β decay and stopped in the active volume of the OTPC detector. The dashed line shows the proton-stopping efficiency as a function of energy. The dotted vertical lines mark the energy intervals corresponding to the proton groups around 1250 keV (900–1400 keV), 1550 keV (1400–1900 keV), and 2050 keV (1900–2300 keV). Lower panel: expanded low-energy portion of the spectrum. The vertical dotted lines mark the energy intervals for the energy of the proton-groups at about 300 keV (150–350 keV) and 600 keV (500–700 keV). See also Table II.

it. The total branching ratio determined in this work is in good agreement with the result of ~92% obtained in the previous work by Blank *et al.* [7]. The missing 10.5% composition of ^{23}Si β decay observed here is most likely due to feeding of the ground state of the ^{23}Al daughter. Such interpretation is supported also by shell-model calculations, as reported in Ref. [7], which give 6% direct decay to the ^{23}Al daughter.

A maximum likelihood fit of the time distribution of all 6179 observed decay events with respect to the time of ion implantation yielded a half-life of 47(1) ms, a slightly higher value than found in literature (42.3(4) ms [7] and 40.2(19) ms [8]).

2. β-delayed proton emission

Among the decay events identified as $\beta 1p$, 3D reconstruction and energy determination could be performed only for

TABLE II. Branching ratios for the observed low-energy βp transitions in the decay of ^{23}Si. The energy regions corresponding to the proton groups are highlighted in Fig. 5. The energy dependence of the detection efficiency and the probability to detect a decay in the finite-time observation window are taken into account in the branching ratio determination. See text.

This work			Literature			
Proton-group			Proton energy		Branching	
energy	Events	Branching	Ref. [7] (keV)	Ref. [8] (keV)	Ref. [7]	Ref. [8]
300	8^{+4}_{-3}	$(0.12^{+0.06}_{-0.04})$%	–	–		
650	8^{+4}_{-3}	$(0.12^{+0.06}_{-0.04})$%	600(60)	673(36)	<3%	2.4(1)%
1250	230±16	(3.6 ± 0.2)%	1320(40)	1346(39)	10(1)%	5.1(4)%
1550	200 ± 15	(4.6 ± 0.3)%	1700(60)	1631(46)	<5%	4.6(6)%
2050	52±8	(4.4 ± 0.7)%	2400(40)	2309(41)	32(2)%	21(2)%

those protons that were fully contained in the active volume of the chamber (585 events). The combined information on length of the track on the CCD image, duration of the PMT signal corresponding to the emitted proton (obtained by fitting the signal with energy-loss distribution [23]) and energy dependence of the particle range for the given gas mixture [23], allowed to reconstruct the momentum of each stopped proton and determine the energy spectrum. For the remaining protons, which escaped the chamber, only a low-energy limit for their energy could be established. This was done on the basis of the proton range calculated simply from the length of the signals in both the CCD and PMT. The quality of the energy determination from the range was verified by comparing the two methods at work on the stopped protons. Moreover, Monte Carlo simulations of the expected energy deposited in the OTPC by protons emitted in the decay of ^{23}Si showed good agreement with the spectrum observed. The simulation assumed as input the proton-energy distribution observed by Blank *et al.* [7]. The uncertainty on the reconstructed proton energy spanned from ∼100 keV at 200 keV, to ∼80 keV at 650 keV, to ∼60 keV at 1000–1500 keV

In Fig. 5 the energy spectrum of βp stopped in the active volume of the OTPC is shown. Five groups of protons could be identified at energies of about 300, 650, 1250, 1550, and 2050 keV. The respective branching ratios are summarised in Table II. The partial decay scheme of ^{23}Si illustrating the experimental knowledge on the ^{23}Al levels fed in β decay and the levels of relevance for ^{23}Si βp decay is shown in Fig. 6.

The group of protons at about 650 keV corresponds most likely to several (weak) transitions, rather than the proton peak at 600(60) keV in Ref. [7] and 673 keV in Ref. [8], in particular if we take into account the small branching ratio observed in this work with respect to the much larger value of 2.4% reported in literature [8]. The group centered around 1250 keV corresponds to the peak at 1320(40) keV in Ref. [7] and 1346(39) keV in Ref. [8], de-exciting the 1475 keV $3/2^+$ level in ^{23}Al [24] to the ground state of ^{22}Mg, see Fig. 6. On the other hand, the group of proton events peaking at about 1550 keV should correspond to the transition at 1700(60) keV in Ref. [7] and 1631(46) keV in Ref. [8], i.e., the decay of the 3166 keV $3/2^+$ level in ^{23}Al [24] to the first excited state in ^{22}Mg at 1247 keV and/or the decay of the 5134 keV $7/2^+$ level in ^{23}Al to the second excited state in ^{22}Mg at 3308 keV. The group of events at 2050 keV may be due to the tail of the proton transition at 2400(40) keV in Ref. [7] and 2309(41) keV in Ref. [8]. The lower branching ratio and proton energy observed here with respect to literature most likely stem from the low stopping efficiency at these energies. The group of protons at about 300 keV energy is observed here for the first time and it is probably due to more than one transition. Unfortunately, it cannot be placed in the level scheme.

3. *β-delayed two-proton emission*

The analysis of the β2p events led to the identification of 22 cases among the 533 identified in which both protons were stopped in the active volume of the chamber. Their energies and momenta were reconstructed by using the range method described in Sec. III A 2. Fitting of the signals gave poor results because of the signal quality combined with the too many free parameters involved when three particles (two protons and the recoil) have to be taken into account. In Fig. 7

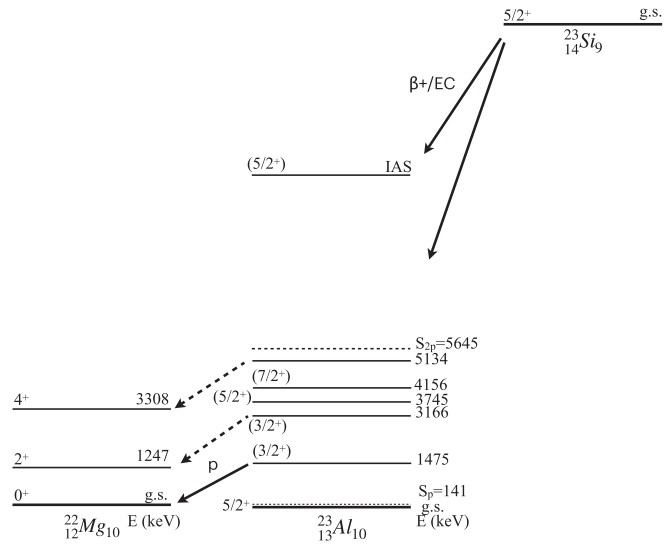

FIG. 6. Partial decay scheme of ^{23}Si illustrating the levels of relevance for its βp decay as found in this work. The proton transitions that could be placed in the decay scheme are marked by arrows. The dashed lines show the two possible transitions for the protons at about 1550 keV energy. All the experimental knowledge available on the ^{23}Al levels fed in β decay completes the picture [24].

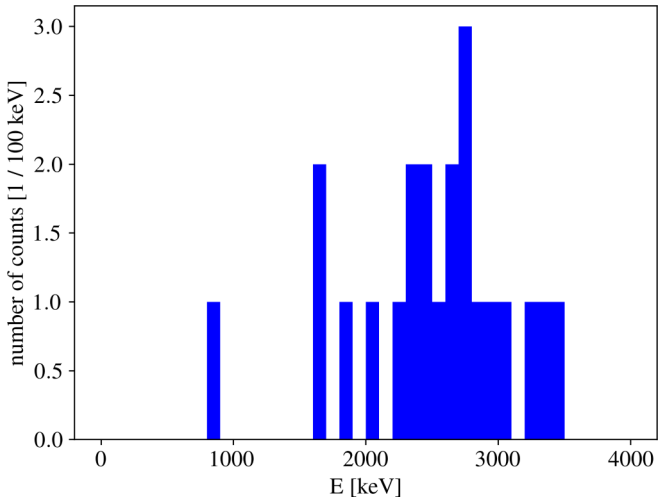

FIG. 7. Sum-energy spectrum of $\beta 2$p events in which both protons stopped in the active volume of the OTPC detector.

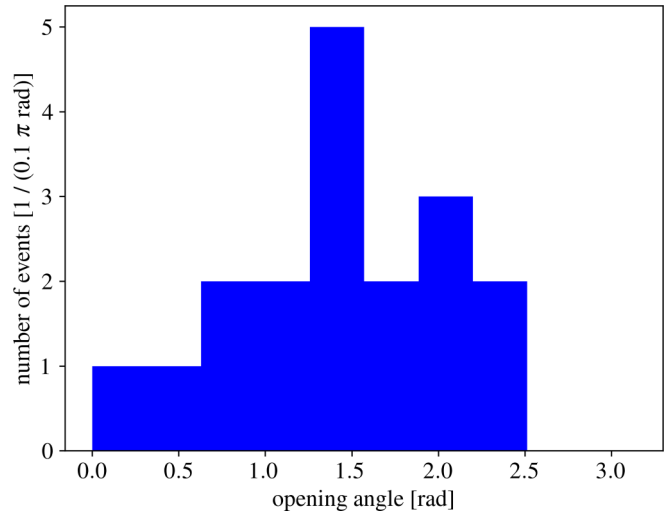

FIG. 9. Opening angle between the two protons for the events shown in Fig. 7 with sum energy above 2 MeV. See text.

the spectrum of the two-protons sum energy is shown. This spectrum shows some structures, which can be interpreted as due to the decay by emission of two protons from level(s) between ∼6550 keV and ∼9000 keV excitation energy in ^{23}Al, providing new information on the structure of this nucleus above S_{2p}. A schematic illustration of the levels involved in the $\beta 2p$ decay of ^{23}Si is given in Fig. 8. The group of counts above 2 MeV sum energy, centered around 2.7 MeV, could originate by β feeding of one broad level at $E_x \sim 8.6$ MeV. On the other hand, it could likely originate from more levels closely spaced in energy, which then decay with prompt emission of two protons. The opening-angle distribution for this group of protons is shown in Fig. 9. Statistical limitations do not allow to fully disentangle the possible different decay paths available, namely simultaneous, diproton, or various sequential emission paths through different, although close in energy, levels in the βp daughter ^{22}Mg. Therefore, it is not possible to determine the decay mechanism at play, although the distribution seems to center rather symmetrically around 90°, which is typical of uncorrelated sequential two-proton emission. The individual energy of each proton in this group is about 1.35 MeV. Assuming GT decay of the ^{23}Si $5/2^+$ ground state to ^{23}Al, $3/2^+$, $5/2^+$, and $7/2^+$ levels will be populated. Taking into consideration emission of low-ℓ

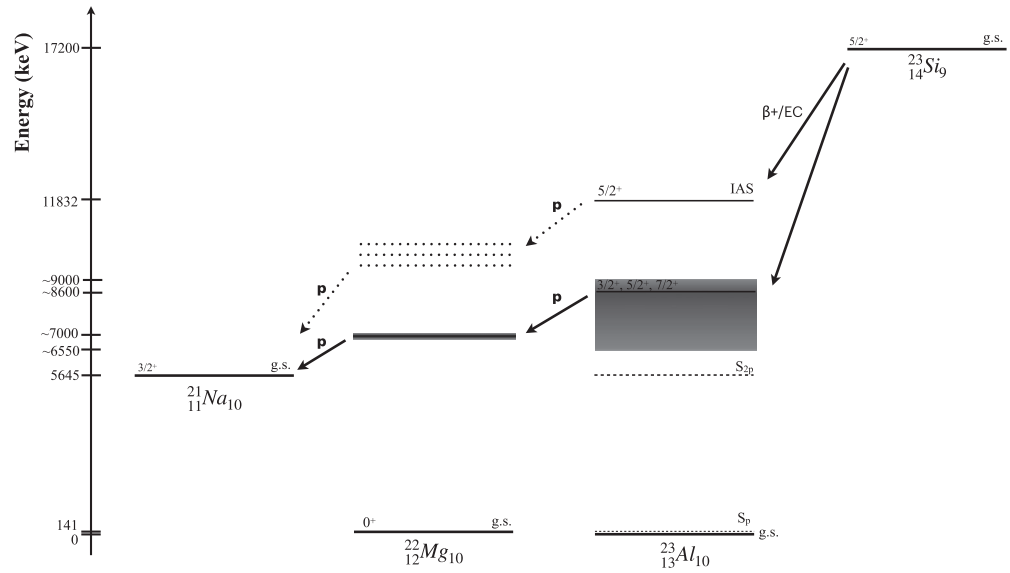

FIG. 8. Partial decay scheme of ^{23}Si illustrating the levels of relevance for its $\beta 2p$ decay. The grey excitation-energy region in ^{23}Al between 6550 and 9000 keV, with level(s) marked by a solid line at ∼8600 keV, show the range of excitation energies from which the two protons shown in Fig. 7 are emitted. Intermediate states in ^{22}Mg at about 7 MeV excitation involved in the process are highlighted. Dashed lines in ^{23}Al show the separation energy for one and for two protons, while dotted lines schematically depict the process of $\beta 2p$ when higher energy protons are emitted (i.e., escaping from the chamber). See text for details.

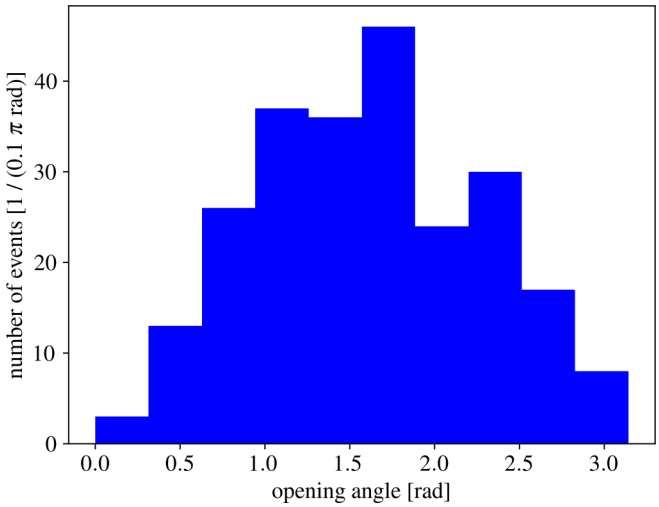

FIG. 10. Opening angle between the two protons for events in which one or both protons escape the chamber. See text.

protons, the decay will proceed through low-spin states in ^{22}Mg at ∼7 MeV excitation energy and subsequent emission of another proton to the $3/2^+$ ground state of ^{21}Na. The data shown in Fig. 7 have therefore a bias due to the fact that at about 1.5 MeV the single-proton detection efficiency drops rapidly with increasing energy (see Fig. 5).

A similar picture present those events in which one or both delayed protons escaped the active volume of the chamber, i.e., events in which protons are emitted from higher-lying excited states. Energy reconstruction was not possible, nevertheless, the opening angle between the two particles could be determined, see Fig. 10.

4. β-delayed three-proton and β-delayed proton-alpha emission

As described in Sec. III A 1, two $\beta 3p$ and one tentative $\beta p\alpha$ event were identified. The analysis of background sources proved that the two β3p events could not be originated by it. In fact, a statistical analysis shows that the probability to observe three random background-events in one 150 ms-long frame is of the order of 3×10^{-6}. Moreover, this low value needs to be folded with the probability that all three events originate at the same time (within less than 1 μs) and at the spot where the ion was implanted. These considerations lead to a negligible probability that the two events are due to background.

One of the $\beta 3p$ events and the βpα event are shown in Fig. 4. A branching ratio $b_{\beta 3p} = (2.9^{+3.8}_{-1.9}) \times 10^{-4}$ was inferred for the former decay mode. The value is along the lines of those for the $\beta 3p$ decay branch from other $T_Z = -5/2$ nuclei, namely, ^{27}S, ^{31}Ar, and ^{43}Cr with $b_{\beta 3p} \leqslant 1 \times 10^{-3}$, $7(2) \times 10^{-4}$, and $(13^{+18}_{-8}) \times 10^{-4}$ [21,25,26], respectively. The only remaining case of $\beta 3p$ decay that is known to date is from the more exotic $T_Z = -7/2$ ^{45}Fe isotope, with a larger $b_{\beta 3p} = 3.3(16) \times 10^{-2}$ [27].

In the case of the $\beta 3p$ decays, it was not possible to univocally determine the energy of each of the particles emitted, but it was possible to determine the range for the sum energy of each of the two events (or its lower limit), by looking at all the possible combinations to pair the tracks on the image with

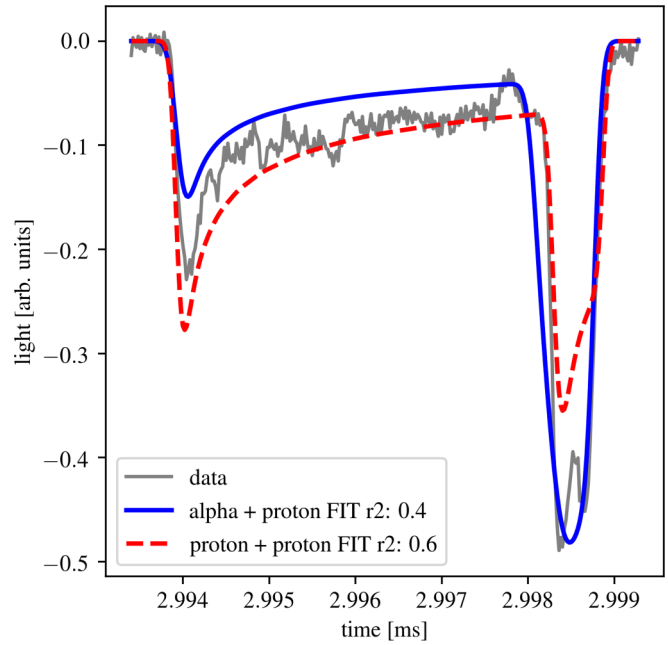

FIG. 11. PMT trace for the event tentatively identified as $\beta\alpha$p decay of ^{23}Al and its fit assuming emission of two protons and one alpha and one proton, respectively. See text for details.

the PMT component. Such analysis led to an average value of 3.65(35) MeV for the event shown in Fig. 4, in which all particles were stopped within the detector active-volume, and a lower limit between 2.7(7) and 3.3(6) MeV for the other event, in which one of the protons escaped. The former event is compatible with the decay of the IAS in ^{23}Al, while the latter may come from the IAS or around it.

The event displayed in Figs. 4(d) and 4(h) was tentatively identified as due to $\beta p\alpha$ emission taking into account several considerations. It was established that the shorter track in the image corresponds to the shorter track in the PMT on the basis of the amount of light. Fitting of the signal was performed, as shown in Fig. 11, by assuming that both tracks are due to protons and that the shorter one is due to an α particle. Given the signal/noise quality, both fits give similar residual (r^2), which is defined here as $r^2 = \sum (\text{fit\_value} - \text{data\_value})^2$, but the proton and α scenario seems to better reproduce the shape of the PMT. The event is therefore tentatively classified as emission of a proton and an α with energies 1.6(1) and 1.2(4) MeV, respectively. The energies of the two particles are in agreement with emission from the IAS in ^{23}Al. In the case of two protons, their energies would be 1.6(1) and 0.4(2) MeV, hence they would be emitted from a state below the IAS. As to the order in which the proton and α are emitted, two are the possible scenarios.

Assuming first emission of an $\ell = 0$ α particle to the ground state of the proton-unbound ^{19}Na nucleus sequentially followed by an $\ell = 2$ proton, the energies available for the α and for the proton would be 3.1 and 0.3 MeV [16], respectively. Decay through excited states in ^{19}Na cannot be excluded *a priori*. Nevertheless, the only candidates known for $5/2^+$ states in ^{19}Na lie at ∼2.5 MeV excitation

energy [28]. This would imply that the α particle had energy of only 0.6 MeV and its emission would be suppressed by the coulomb barrier. Larger-ℓ α transitions are not considered here because of double-hindrance in the barrier penetrability due to the lower energy and larger angular momentum involved in such transition. On the other hand, in the opposite scenario, the proton could feed a highly excited state in ^{22}Mg at about 10.4 MeV with sequential emission of the α particle to the ^{18}Ne ground state. Taking into account the barrier-penetrability dependence on the energy and on the angular momentum, $p+\alpha$ emission from the IAS will involve most likely particles with minimum angular momentum. Several low-spin levels are known in ^{22}Mg at $E_x = 10$–11 MeV from transfer reaction studies [28], including ^{18}Ne$(\alpha, p)^{21}$Na [29], the indirect process to βp emission to the same level in ^{22}Mg. These states could participate in the $\beta p\alpha$ decay allowing for, e.g., $\ell = 1$ protons followed by $\ell = 0$ α particles with energies compatible with those observed. The most likely scenario is the latter, i.e., β decay followed by a proton and subsequent α particle. The first scenario is still possible, though not detected here, given the statistics of only one event observed.

In the previously known three cases for $\beta\alpha p/\beta p\alpha$ emission (^{9}C, ^{17}Ne, and ^{21}Mg [5,30,31]) the mother nuclei had $T_Z = -3/2$ and the decay proceeded through an α-conjugate nucleus (^{8}Be, ^{16}O, and ^{20}Ne). The missing $T_Z = -3/2$ member of this sequence, ^{13}O, decays via ^{12}C. ^{13}O is a candidate for this decay mode with predicted branching ratio of $0.9(3) \times 10^{-4}$ [5]. Both decay sequences were observed in ^{17}Ne with $b_{\beta\alpha p+\beta p\alpha} = 1.6(4) \times 10^{-4}$ and ^{9}C decay. The latter being a special case given the fact that its β daughter is breaking up into a proton and two α particles [30]. In the case of ^{21}Mg, only $\beta p\alpha$ decay was observed with $b_{\beta p\alpha} = 1.6(3) \times 10^{-4}$ [5]. In their work, Lund *et al.* [5] discuss the systematics of β-delayed (multi)particle decays for $T_Z \leqslant -3/2$ and conclude that the presence of these exotic decay modes is due to odd-even effects on the decay energy rather than structure such as α clustering, despite the fact that α-conjugate nuclei are involved in the decay process. They also suggest that the observation of such exotic decay modes as $\beta 3p$ and $\beta p\alpha/\beta\alpha p$ in heavier $T_Z = -5/2$ nuclei ^{23}Si, ^{27}S, ^{31}Ar, etc., would allow to test their interpretation. The discovery of $\beta 3p$ and, tentatively, of $\beta p\alpha$ decay branches of ^{23}Si reported here, together with the known $\beta 3p$ emission from ^{31}Ar [25,32] and ^{43}Cr [26] supports their conclusions on the influence of odd-even effects in the decay energy on the occurrence of these exotic decay modes.

5. DFT *calculations*

The β decay of ^{23}Si was already investigated using state-of-the-art shell-model (SM) approach. The results published in Ref. [7] show that the SM provides a sufficiently accurate description of the low-energy spectrum of ^{23}Al. Hence, instead of repeating the SM calculations, we have decided to use here an alternative approach and perform the multireference density-functional-rooted (DFT-rooted) calculations. The employed method is an extension of the conventional mean-field or single reference density functional theory that restores the violated symmetries and mixes good symmetry states projected from different mean-field configurations. The specific model used here, called DFT-rooted no-core configuration interaction (DFT-NCCI), is described in Ref. [33]. It restores angular momentum and treats properly isospin symmetry, both broken spontaneously by mean-field solutions.

The DFT-NCCI model belongs to a class of the so called *global models*, applicable to predicting the properties of a broad range nuclei. As such, it cannot compete with SM, fine-tuned to the valence space, concerning precision of theoretical predictions. Hence, by performing the DFT-NCCI calculations we do not expect to improve the theoretical description of ^{23}Al, but rather aim to validate the new approach in the nucleus where benchmark SM results exist and test the properties of the underlying functional in this mass region without applying any local adjustment of its parameters.

The model was applied to the investigation of the β-decay pattern for the ground state of ^{23}Si. In the calculations we used the $\mathrm{SV_{SO}}$ density-independent Skyrme interaction [34,35] both to compute the configuration space as well as in the configuration-mixing calculations. The configuration space consisted of the ground state and the two lowest particle-hole configurations in the ^{23}Si and the ground state and 13 excited configurations in the daughter nucleus ^{23}Al. The configuration space was selected in such a way that enabled us to obtain relatively well converged solutions for the ground states of ^{23}Si and ^{23}Al, the low-lying excited states in ^{23}Al with excitation energies below $\approx$3.5 MeV, and the IAS in ^{23}Al. The configurations used in the calculations of the ^{23}Al are described in detail in the Supplemental Material [36]. The adopted configuration space is too small to guarantee a convergence and completeness of the calculated spectrum above 3.5 MeV.

The calculated binding energies for the $I^\pi = 5/2^+$ ^{23}Si and ^{23}Al ground states are 158.2 MeV and 172.7 MeV, and are 4.8% and 2.4% larger than the experimental binding energies of 150.735 MeV and 168.719 MeV [16], respectively. Besides the $5/2^+$ ground states, the calculations for ^{23}Al yielded an $I^\pi = 7/2^+$ $E_x = 1.33$ MeV first excited state, followed by $I^\pi = 1/2^+$ at $E_x = 1.48$ MeV, $I^\pi = 3/2^+$ at $E_x = 1.72$ MeV, $I^\pi = 5/2^+_1$ at $E_x = 2.83$ MeV, and the second excited $I^\pi = 7/2^+$ state at $E_x = 3.18$ MeV The calculated spectrum is depicted in Fig. 12. At low energies it compares relatively well with the shell-model (SM) results of Ref. [7].

The same calculations yielded an excitation energy of 9.27 MeV for the $5/2^+$ IAS of ^{23}Si in ^{23}Al, somewhat lower than the experimental value of 11.78 MeV [7]. The discrepancy may indicate a need for better calibration of the symmetry energy strength in the $\mathrm{SV_{SO}}$ functional. As expected, decay to the IAS dominates, with matrix elements $|M_\mathrm{F}| \approx \sqrt{4.9}$ and $|M_\mathrm{GT}| \approx 1.5$ for Fermi and GT decays, respectively. GT decay is predicted to populate mostly states at excitation energies of 5.8 MeV ($I^\pi = 5/2^+$) and 7.8 MeV ($I^\pi = 7/2^+$) with matrix elements $|M_\mathrm{GT}| = 1.3$ and 1.6, respectively. It seems to be at variance with the shell-model calculation of Ref. [7] which predicts strong decays to the 3.83 MeV $5/2^+$ and 3.24 MeV $3/2^+$ states. Let us stress, however, that our conclusion concerning the GT matrix elements can change since, as mentioned above, the spectrum may be incomplete in the energy range $E_x \geqslant 3.5$ MeV due to limitations in the size of the adopted configuration space. At present, we

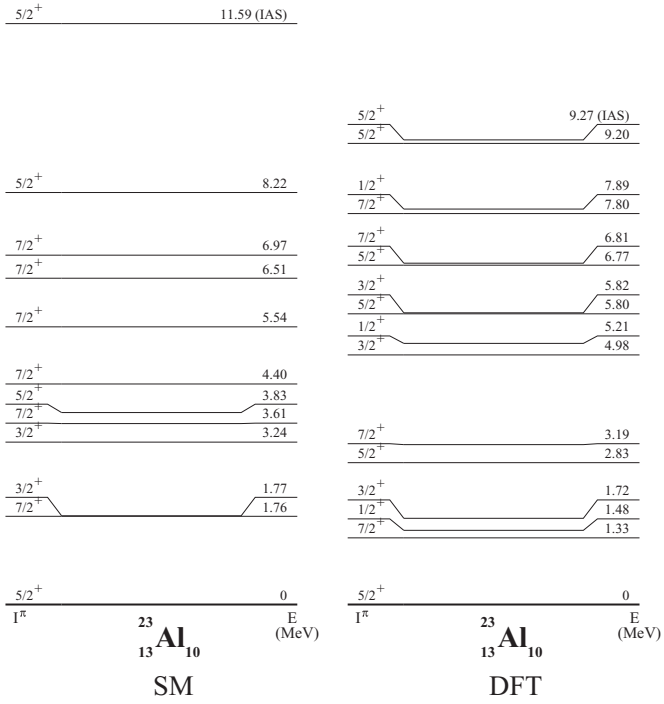

FIG. 12. Excitation energy spectrum for low lying states and the IAS in ^{23}Al from DFT (this work) and shell model (SM) of Ref. [7]. See text for details.

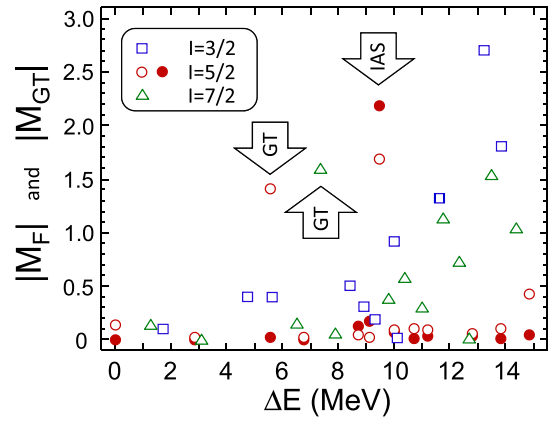

FIG. 13. Matrix elements for the g.s. β decay of ^{23}Si calculated within the DFT-NCCI variant that involves only AMP. Filled (open) symbols label Fermi (GT) matrix elements, respectively. Triangles, circles, and squares mark GT matrix elements between the g.s. of ^{23}Si and $I = 3/2^+, 5/2^+$, and $7/2^+$ states in ^{23}Al below 15 MeV. Arrows show IAS and low-lying states strongly populated by the GT decay which are discussed in the text.

can safely state that the GT decay to the lowest-lying states with $E_x < 3$ MeV give matrix-element values well below unity.

The hindrance of the calculated GT matrix elements and dominance of the IAS in the decay pattern of ^{23}Si can be explained by the shape difference predicted for ^{23}Si (weakly deformed oblate) and ^{23}Al (well deformed prolate). The calculated mean quadrupole deformation parameters are $\beta_2 = 0.090$, $\gamma = 60^\circ$ for the g.s. configuration in ^{23}Si and $\beta_2 = 0.345$, $\gamma = 0^\circ$ for the g.s. configuration in ^{23}Al. The lowest p-h excitations in ^{23}Al are also well deformed.

All calculations presented in this work were done using the HFODD solver [37,38] equipped with the DFT-NCCI module. In the calculations we used the basis composed of ten spherical HO shells. The exchange term of the Coulomb interaction was treated exactly.

The stability of the calculations presented above was verified by angular-momentum-projected (AMP) calculations, which allow to include more configurations and verify the stability of low-energy spectra predictions, wave functions and β-decay rates. In this variant of the calculations we extended the configuration space to 32 self-consistent mean-field solutions. The results of these calculations are shown in Fig. 13 which summarizes the calculated matrix elements for Fermi and Gamow-Teller β decay of the g.s. in ^{23}Si.

The DFT-NCCI-AMP results are fully consistent with the DFT-NCCI calculations presented above that involve both the isospin- and angular-momentum projections. Both sets of DFT-NCCI calculations are at variance with the shell-model calculation of Ref. [7] which, as already mentioned, predicts strong decays to the 3.83 MeV $5/2^+$ and 3.24 MeV $3/2^+$ states. The reason for the discrepancy is not clear and require further studies and better calibration of the functional. Such study is beyond the scope of the present work. The readers who are interested in further details concerning the DFT-NCCI-AMP calculations are referred to the Supplemental Material which is an integral part of this work [36].

B. ^{22}Si

Events corresponding to ^{22}Si ions which triggered the data acquisition and stopped in the active volume of the detector were considered for further analysis. The same procedure employed in the identification of well implanted ^{23}Si ions was used, see Sec. III A 1. A total of 63 ^{22}Si ions met these requirements. The analysis allowed to confirm the decay pattern for this isotope, namely, decay with emission of one and two delayed protons. Example decay events with particle emission are shown in Fig. 14 and the statistics collected is summarized in Table III. The branching ratios values take into account the finite-time observation window, which gives a 97.1(6)% probability to observe any ^{22}Si decay within it.

A maximum likelihood fit of the time distribution of the decay events observed with respect to the time of ion implantation yielded a half-life of $24(^{+4}_{-3})$ ms, in

TABLE III. The total branching ratios for the observed decay channels of ^{22}Si.

channel	Events	Branching
β1p	58	$95(^{+14}_{-12})$%
β2p	2	$3(^{+4}_{-2})$%

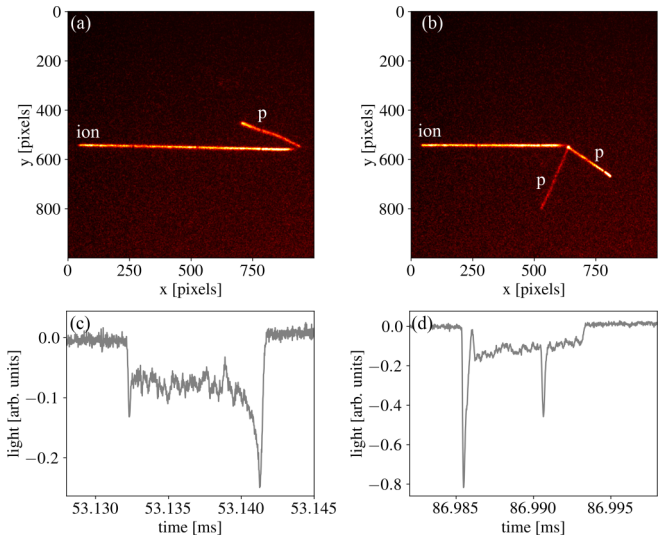

FIG. 14. Top panels: CCD images for example events of (a) βp and (b) $\beta 2p$ decay of ^{22}Si. The horizontal track from left to right in each image corresponds to the ^{22}Si ion entering the chamber. The tracks emerging from the ion stopping point correspond to the emitted particles. Bottom panels: respective PMT signals for the (c) βp and (d) $\beta 2p$ decay events. The signal generated by the ^{22}Si ion stopped in the chamber is not visible in the histograms displayed in the bottom panels. Only the portion of the PMT signal centered around the time at which the decay happened is shown. When a single particle is recorded in the decay, the PMT signal shows the corresponding Bragg peak. In the βp event in (a) and (c), the proton was emitted upwards, towards the cathode. In the case of more particles emitted at the same time, as is for $\beta 2p$, the PMT signal will be the convolution of the signals corresponding to each of the particles emitted.

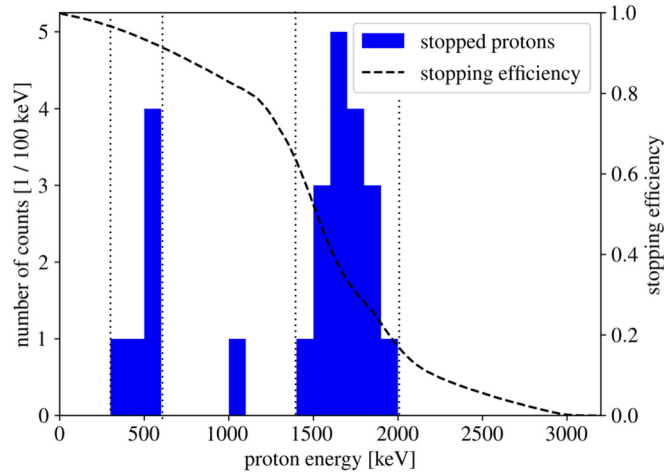

FIG. 15. Energy spectrum for protons following ^{22}Si β decay and stopped in the active volume of the OTPC detector. The dashed line shows the proton-stopping efficiency as a function of energy. The vertical dotted lines mark the energy intervals for the proton-groups reported in Table III.

agreement with literature (29(2) ms [13], 27.8(35) ms [14], and 28.6(14) ms [15]).

The analysis of the βp events allowed to classify 24 of them as stopped within the active volume of the detector. Their energies were reconstructed and the distribution is shown in Fig. 15. Two groups of low-energy protons can be clearly identified at 0.6(1) MeV and 1.7(1) MeV with total branching ratios of $(10^{+6}_{-4})\%$ and $(77^{+27}_{-22})\%$, respectively. The former corresponds to the proton group at 680(50) keV [14] or 710(50) keV [15], while the latter could be due to the low-energy tail of the two protons transitions at 1950(50) and 2150(50) keV [15].

As far as $\beta 2p$ decay events are concerned, in both cases one of the two protons escaped the detector, therefore the energy could not be reconstructed. The total branching ratio for this decay mode was calculated to be $(3^{+4}_{-2})\%$. This is in accordance with the lower limit of $b^{IAS}_{\beta 2p} = 0.7(3)\%$ inferred for it in Ref. [15].

IV. SUMMARY

β-delayed charged particle emission from ^{23}Si and ^{22}Si was studied at the focal plane of the MARS spectrometer at the Cyclotron Institute of Texas A&M University with a time-projection chamber with optical readout. One new decay mode, namely $\beta 3p$, was discovered for ^{23}Si and another, $\beta p\alpha$, tentatively identified. Moreover, the absolute branching ratios were determined for all decay branches, a new low-energy βp transition was identified and $\beta 2p$ emission through levels well below the IAS was observed.

These kind of investigations are very well suited for testing symmetry energies. In this context, DFT-rooted configuration-interaction calculations were performed to investigate the β-decay pattern of ^{23}Si. According to the calculations, the β-decay pattern is completely dominated by the IAS. Decay to the states below the IAS is predicted to be hindered due to the shape difference of ^{23}Si (weakly deformed oblate) and ^{23}Al (well deformed prolate). Within the considered configuration space, the largest are GT matrix elements to the $I^\pi = 5/2^+$ $(7/2^+)$ states at excitation energies 5.8 (7.8) MeV, respectively. GT matrix elements to other states, in particular to the lowest states, are well below unity. The excitation energy of the IAS is underestimated, fact which may indicate a need for better calibration of the symmetry energy strength.

The study of ^{22}Si allowed to establish the absolute decay branch for $\beta 2p$ emission. Further studies with larger statistics are needed in order to shed light into the mechanism of $\beta 2p$ emission.

ACKNOWLEDGMENTS

This work was supported by the National Science Centre, Poland, under Contracts No. 2015/17/B/ST2/00581, No. 2015/16/S/ST2/00423, No. 2019/33/B/ST2/02908, and No. 2018/31/B/ST2/02220, and Department of Energy, Office of Science, under Award No. DE-FG02-93ER40773. A.A.C. acknowledges support by the Polish Ministry of Science and Higher Education through Grant No. 0079/DIA/2014/43 (Grant Diamentowy).

[1] B. Blank and M. Borge, Prog. Part. Nucl. Phys. **60**, 403 (2008).

[2] M. Pfützner, M. Karny, L. V. Grigorenko, and K. Riisager, Rev. Mod. Phys. **84**, 567 (2012).

[3] G. Koldste, B. Blank, M. Borge, J. Briz, M. Carmona-Gallardo, L. Fraile, H. Fynbo, J. Giovinazzo, J. Johansen, A. Jokinen, B. Jonson, T. Kurturkian-Nieto, T. Nilsson, A. Perea, V. Pesudo, E. Picado, K. Riisager, A. Saastamoinen, O. Tengblad, J.-C. Thomas, and J. Van de Walle, Phys. Lett. B **737**, 383 (2014).

[4] H. Fynbo, M. Borge, L. Axelsson, J. Äystö, U. Bergmann, L. Fraile, A. Honkanen, P. Hornshøj, Y. Jading, A. Jokinen, B. Jonson, I. Martel, I. Mukha, T. Nilsson, G. Nyman, M. Oinonen, I. Piqueras, K. Riisager, T. Siiskonen, M. Smedberg, O. Tengblad, J. Thaysen, and F. Wenander, Nucl. Phys. A **677**, 38 (2000).

[5] M. Lund, M. Borge, J. Briz, J. Cederkall, H. Fynbo, J. Jensen, B. Jonson, K. Laursen, T. Nilsson, A. Perea, V. Pesudo, K. Riisager, and O. Tengblad, Phys. Lett. B **750**, 356 (2015).

[6] M. Langevin, A. Mueller, D. Guillemaud-Mueller, M. Saint-Laurent, R. Anne, M. Bernas, J. Galin, D. Guerreau, J. Jacmart, S. Hoath, F. Naulin, F. Pougheon, E. Quiniou, and C. Détraz, Nucl. Phys. A **455**, 149 (1986).

[7] B. Blank, F. Boué, S. Andriamonje, S. Czajkowski, R. Del Moral, J. P. Dufour, A. Fleury, P. Pourre, M. S. Pravikoff, E. Hanelt, N. A. Orr, and K. H. Schmidt, Z. Phys. A Hadrons and Nuclei **357**, 247 (1997).

[8] K. Wang, D. Q. Fang, Y. T. Wang, X. X. Xu, L. J. Sun, Z. Bai, M. R. Huang, S. L. Jin, C. Li, H. Li, J. Li, X. F. Li, C. J. Lin, J. B. Ma, P. Ma, W. H. Ma, M. W. Nie, C. Z. Shi, H. W. Wang, J. G. Wang, J. S. Wang, L. Yang, Y. Y. Yang, H. Q. Zhang, Y. J. Zhou, Y. G. Ma, and W. Q. Shen, Int. J. Mod. Phys. E **27**, 1850014 (2018).

[9] J. J. He, S. Kubono, T. Teranishi, M. Notani, H. Baba, S. Nishimura, J. Y. Moon, M. Nishimura, H. Iwasaki, Y. Yanagisawa, N. Hokoiwa, M. Kibe, J. H. Lee, S. Kato, Y. Gono, and C. S. Lee, Phys. Rev. C **76**, 055802 (2007).

[10] T. Gomi, T. Motobayashi, Y. Ando, N. Aoi, H. Baba, K. Demichi, Z. Elekes, N. Fukuda, Z. Fulop, U. Futakami, H. Hasegawa, Y. Higurashi, K. Ieki, N. Imai, M. Ishihara, K. Ishikawa, N. Iwasa, H. Iwasaki, S. Kanno, Y. Kondo, T. Kubo, S. Kubono, M. Kunibu, K. Kurita, Y. Matsuyama, S. Michimasa, T. Minemura, M. Miura, H. Murakami, T. Nakamura, M. Notani, S. Ota, A. Saito, H. Sakurai, M. Serata, S. Shimoura, T. Sugimoto, E. Takeshita, S. Takeuchi, Y. Togano, K. Ue, K. Yamada, Y. Yanagisawa, and K. Yoneda, Nucl. Phys. A **758**, 761 (2005), nuclei in the Cosmos VIII.

[11] J. A. Caggiano, D. Bazin, W. Benenson, B. Davids, R. Ibbotson, H. Scheit, B. M. Sherrill, M. Steiner, J. Yurkon, A. F. Zeller, B. Blank, M. Chartier, J. Greene, J. A. Nolen, A. H. Wuosmaa, M. Bhattacharya, A. Garcia, and M. Wiescher, Phys. Rev. C **64**, 025802 (2001).

[12] M. G. Saint-Laurent, J. P. Dufour, R. Anne, D. Bazin, V. Borrel, H. Delagrange, C. Détraz, D. Guillemaud-Mueller, F. Hubert, J. C. Jacmart, A. C. Mueller, F. Pougheon, M. S. Pravikoff, and E. Roeckl, Phys. Rev. Lett. **59**, 33 (1987).

[13] B. Blank, S. Andriamonje, F. Boué, S. Czajkowski, R. Del Moral, J. P. Dufour, A. Fleury, P. Pourre, M. S. Pravikoff, K.-H. Schmidt, E. Hanelt, and N. A. Orr, Phys. Rev. C **54**, 572 (1996).

[14] X. Xu, C. Lin, L. Sun, J. Wang, Y. Lam, J. Lee, D. Fang, Z. Li, N. Smirnova, C. Yuan, L. Yang, Y. Wang, J. Li, N. Ma, K. Wang, H. Zang, H. Wang, C. Li, M. Liu, J. Wang, C. Shi, M. Nie, X. Li, H. Li, J. Ma, P. Ma, S. Jin, M. Huang, Z. Bai, F. Yang, H. Jia, Z. Liu, D. Wang, Y. Yang, Y. Zhou, W. Ma, J. Chen, Z. Hu, M. Wang, Y. Zhang, X. Ma, X. Zhou, Y. Ma, H. Xu, G. Xiao, and H. Zhang, Phys. Lett. B **766**, 312 (2017).

[15] J. Lee, X. X. Xu, K. Kaneko, Y. Sun, C. J. Lin, L. J. Sun, P. F. Liang, Z. H. Li, J. Li, H. Y. Wu, D. Q. Fang, J. S. Wang, Y. Y. Yang, C. X. Yuan, Y. H. Lam, Y. T. Wang, K. Wang, J. G. Wang, J. B. Ma, J. J. Liu, P. J. Li, Q. Q. Zhao, L. Yang, N. R. Ma, D. X. Wang, F. P. Zhong, S. H. Zhong, F. Yang, H. M. Jia, P. W. Wen, M. Pan, H. L. Zang, X. Wang, C. G. Wu, D. W. Luo, H. W. Wang, C. Li, C. Z. Shi, M. W. Nie, X. F. Li, H. Li, P. Ma, Q. Hu, G. Z. Shi, S. L. Jin, M. R. Huang, Z. Bai, Y. J. Zhou, W. H. Ma, F. F. Duan, S. Y. Jin, Q. R. Gao, X. H. Zhou, Z. G. Hu, M. Wang, M. L. Liu, R. F. Chen, and X. W. Ma (RIBLL Collaboration), Phys. Rev. Lett. **125**, 192503 (2020).

[16] M. Wang, W. Huang, F. Kondev, G. Audi, and S. Naimi, Chin. Phys. C **45**, 030003 (2021).

[17] M. Antony, A. Pape, and J. Britz, At. Data Nucl. Data Tables **66**, 1 (1997).

[18] R. Tribble, R. Burch, and C. Gagliardi, Nucl. Instrum. Methods Phys. Res. A **285**, 441 (1989).

[19] A. Saastamoinen, L. Trache, A. Banu, M. A. Bentley, T. Davinson, J. C. Hardy, V. E. Iacob, M. McCleskey, B. T. Roeder, E. Simmons, G. Tabacaru, R. E. Tribble, P. J. Woods, and J. Äystö, Phys. Rev. C **83**, 045808 (2011).

[20] A. A. Ciemny, W. Dominik, T. Ginter, R. Grzywacz, Z. Janas, M. Kuich, C. Mazzocchi, K. Miernik, M. Pfützner, M. Pomorski, D. Bazin, T. Baumann, A. Bezbakh, B. P. Crider, M. Ćwiok, S. Go, G. Kamiński, K. Kolos, A. Korgul, E. Kwan, S. N. Liddick, S. V. Paulauskas, J. Pereira, K. P. Rykaczewski, C. Sumithrarachchi, and Y. Xiao, Eur. Phys. J. A **52**, 89 (2016).

[21] Ł. Janiak, N. Sokołowska, A. A. Bezbakh, A. A. Ciemny, H. Czyrkowski, R. Dąbrowski, W. Dominik, A. S. Fomichev, M. S. Golovkov, A. V. Gorshkov, Z. Janas, G. Kamiński, A. G. Knyazev, S. A. Krupko, M. Kuich, C. Mazzocchi, M. Mentel, M. Pfützner, P. Pluciński, M. Pomorski, R. S. Slepniev, and B. Zalewski, Phys. Rev. C **95**, 034315 (2017).

[22] F. Sauli, Nucl. Instrum. Methods Phys. Res. A **580**, 971 (2007), imaging 2006.

[23] www.srim.org.

[24] M. Shamsuzzoha Basunia and A. Chakraborty, Nucl. Data Sheets **171**, 1 (2021).

[25] A. A. Lis, C. Mazzocchi, W. Dominik, Z. Janas, M. Pfützner, M. Pomorski, L. Acosta, S. Baraeva, E. Casarejos, J. Duénas-Díaz, V. Dunin, J. M. Espino, A. Estrade, F. Farinon, A. Fomichev, H. Geissel, A. Gorshkov, G. Kamiński, O. Kiselev, R. Knöbel, S. Krupko, M. Kuich, Y. A. Litvinov, G. Marquinez-Durán, I. Martel, I. Mukha, C. Nociforo, A. K. Ordúz, S. Pietri, A. Prochazka, A. M. Sánchez-Benítez, H. Simon, B. Sitar, R. Slepnev, M. Stanoiu, P. Strmen, I. Szarka, M. Takechi, Y. Tanaka, H. Weick, and J. S. Winfield, Phys. Rev. C **91**, 064309 (2015).

[26] M. Pomorski, K. Miernik, W. Dominik, Z. Janas, M. Pfützner, C. R. Bingham, H. Czyrkowski, M. Ćwiok, I. G. Darby, R. Dąbrowski, T. Ginter, R. Grzywacz, M. Karny, A. Korgul, W. Kuśmierz, S. N. Liddick, M. Rajabali, K. Rykaczewski, and A. Stolz, Phys. Rev. C **83**, 014306 (2011).

[27] K. Miernik, W. Dominik, Z. Janas, M. Pfützner, C. R. Bingham, H. Czyrkowski, M. Ćwiok, I. G. Darby, R. Dąbrowski, T. Ginter, R. Grzywacz, M. Karny, A. Korgul, W. Kuśmierz, S. N. Liddick, M. Rajabali, K. Rykaczewski, and A. Stolz, Phys. Rev. C **76**, 041304(R) (2007).

[28] www.nndc.bnl.gov.
[29] M. S. Basunia, Nucl. Data Sheets **127**, 69 (2015).
[30] E. Gete, L. Buchmann, R. E. Azuma, D. Anthony, N. Bateman, J. C. Chow, J. M. D'Auria, M. Dombsky, U. Giesen, C. Iliadis, K. P. Jackson, J. D. King, D. F. Measday, and A. C. Morton, Phys. Rev. C **61**, 064310 (2000).
[31] J. C. Chow, J. D. King, N. P. T. Bateman, R. N. Boyd, L. Buchmann, J. M. D'Auria, T. Davinson, M. Dombsky, E. Gete, U. Giesen, C. Iliadis, K. P. Jackson, A. C. Morton, J. Powell, and A. Shotter, Phys. Rev. C **66**, 064316 (2002).
[32] G. T. Koldste, B. Blank, M. J. G. Borge, J. A. Briz, M. Carmona-Gallardo, L. M. Fraile, H. O. U. Fynbo, J. Giovinazzo, B. D. Grann, J. G. Johansen, A. Jokinen, B. Jonson, T. Kurturkian-Nieto, J. H. Kusk, T. Nilsson, A. Perea, V. Pesudo, E. Picado, K. Riisager, A. Saastamoinen, O. Tengblad, J.-C. Thomas, and J. Van de Walle, Phys. Rev. C **89**, 064315 (2014).
[33] W. Satuła, P. Bączyk, J. Dobaczewski, and M. Konieczka, Phys. Rev. C **94**, 024306 (2016).
[34] M. Beiner, H. Flocard, N. Van Giai, and P. Quentin, Nucl. Phys. A **238**, 29 (1975).
[35] M. Konieczka, P. Bączyk, and W. Satuła, Phys. Rev. C **93**, 042501(R) (2016).
[36] See Supplemental Material at http://link.aps.org/supplemental/10.1103/PhysRevC.106.014317 for a detailed description of the calculations.
[37] J. Dobaczewski, W. Satuła, B. Carlsson, J. Engel, P. Olbratowski, P. Powałowski, M. Sadziak, J. Sarich, N. Schunck, A. Staszczak, M. Stoitsov, M. Zalewski, and H. Zduńczuk, Comput. Phys. Commun. **180**, 2361 (2009).
[38] N. Schunck, J. Dobaczewski, W. Satuła, P. Bączyk, J. Dudek, Y. Gao, M. Konieczka, K. Sato, Y. Shi, X. Wang, and T. Werner, Comput. Phys. Commun. **216**, 145 (2017).